Applied Catalysis B: Environment and Energy 363 (2025) 124803

Contents lists available at ScienceDirect

Applied Catalysis B: Environment and Energy

journal homepage: www.elsevier.com/locate/apcatb

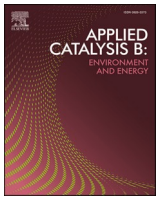

Pore accessibility matters in CO_2 electrolysis: Preventing H_2 formation and boosting triple-phase boundary on microtubular gas-diffusion electrodes

Guoliang Chen [a], Lei Ge [a,b,*], Beibei Ma [c], Yizhu Kuang [a], Hesamoddin Rabiee [a,c,d,*], Fatereh Dorosti [c], Ashok Kumar Nanjundan [a,b], Zhonghua Zhu [c], Hao Wang [a,b,*]

[a] Centre for Future Materials, University of Southern Queensland, Springfield, QLD 4300, Australia
[b] School of Engineering, University of Southern Queensland, Springfield, QLD 4300, Australia
[c] School of Chemical Engineering, The University of Queensland, Brisbane, QLD 4072, Australia
[d] University of Bern, Department of Chemistry, Biochemistry and Pharmaceutical Sciences, Freiestrasse 3, Bern 3012, Switzerland

ARTICLE INFO

Keywords:
Electrochemical reduction of CO_2
Microtubular gas-diffusion electrode
CO_2 gas distribution
Triple-phase boundary
Microenvironment tuning

ABSTRACT

The availability of CO_2 near the active sites is crucial for suppressing hydrogen evolution reaction (HER) and improving the kinetics of electrochemical reduction of CO_2 (CO_2RR) in aqueous electrolytes at high current density. The hollow fiber gas-diffusion electrodes (HFGDEs) configuration can deliver CO_2 continuously to catalyst/electrolyte interfaces without requiring a separate gas chamber, contrasting with planar gas-diffusion electrodes (GDEs). However, the relatively inhomogeneous pore geometry on the surface of HFGDEs leads to poor CO_2 distribution, resulting in an increasing number of flooded pores and parasitic HER, especially at high current densities. This work presents a facile strategy to enhance CO_2 distribution and optimize triple-phase boundary formation by manipulating the surface wettability of HFGDEs. The infiltration and melting of hydrophobic agents (e.g., polytetrafluoroethylene (PTFE)) have been carried out on the Zn nanosheet-deposited Cu hollow fiber. The fluorescent residue area (water surface coverage) with a ~66.7 % decrease and the observation of CO_2 bubbling enhancement confirmed the improvement of CO_2 distribution on HFGDE, and the resulting HFGDE achieved around ~39 % increase in terms of industrial-scale CO partial current density and 4 times higher stability compared to the pristine HFGDE. This research highlights the use of HFGDEs to achieve gas flow-through, further combining with a versatile strategy to enhance CO_2 distribution which can be applied for other gas-phase electrolysis reactions through creating improved triple-phase interfaces and maximizing reaction activity.

1. Introduction

Storing renewable electricity into value-added chemicals via electrochemical reduction reaction of CO_2 (CO_2RR) is an effective strategy for mitigating carbon emissions and reducing conventional feedstock consumption [1,2]. Among the diverse array of CO_2RR products, carbon monoxide (CO) garners significant attention as a crucial raw chemical for industrial processes, including the Fischer-Tropsch [3]. However, a key challenge for the electrochemical conversion of CO_2 to CO is that the competitive hydrogen evolution reaction (HER) also occurs at the same potential range as CO_2RR. Therefore, numerous efforts have been devoted to developing advanced electrocatalysts with high intrinsic activity and selectivity for CO production [4–8]. Most of the electrocatalysts for CO production were performed in H-Cell with limited current densities around of 10 mA/cm^2. The low current density of electrocatalysts performed in H-Cell [7–11] is mainly attributed to the deprived CO_2 local concentration near the electrode and mass transportation resistance, as CO_2 diffuses from bulk electrolytes to catalyst/electrolyte interfaces.

To improve the current density and address the issue of CO_2 diffusion, gas diffusion electrodes (GDEs) were applied by incorporating flow cells working under alkaline conditions to achieve the industrial-scale current density over 200 mA/cm^2 [8,12–14]. The GDEs enable CO_2 to quickly diffuse to the active sites, thus accelerating mass transfer and improving reaction kinetics. The improved current density in the GDE condition results from a shorter diffusion path, in which from the CO_2 gas phase to the catalyst surface is approximately 50 nm [15,16], whereas in the case of non-GDE condition, it is about 50 μm from bulk

* Corresponding authors at: Centre for Future Materials, University of Southern Queensland, Springfield, QLD 4300, Australia.
E-mail addresses: lei.ge@usq.edu.au (L. Ge), hesamoddin.rabiee@unibe.ch (H. Rabiee), hao.wang@usq.edu.au (H. Wang).

https://doi.org/10.1016/j.apcatb.2024.124803
Received 2 September 2024; Received in revised form 3 November 2024; Accepted 8 November 2024
Available online 10 November 2024

electrolytes to electrodes [15]. However, GDEs in such conditions suffer from salt precipitation and decreased hydrophobicity, leading to the blockage of mass transfer channels and flooding, degrading their stability and performance [17]. Despite enormous efforts, GDEs are still suffering from stability issues under the cathodic conditions of CO_2RR. Moreover, the complexity of assembling a planar GDE limits its industrial application as it requires a separated gas chamber, a super hydrophobic gas diffusion layer, a microporous layer, and a catalyst layer.

Recently, hollow fiber (microtubular) gas-diffusion electrodes have emerged as promising electrode configurations for CO_2RR [18–23]. The HFGDE could reduce the complexity of the cell by utilizing the lumen side of the hollow fiber as a gas chamber, and the CO_2 gas can be directly fed into the inner chamber to penetrate through the hollow fiber walls, thus providing sufficient CO_2 near the catalytic sites. The cylindrical HFGDE with a high surface area-to-volume ratio can load various and dense electrocatalysts for CO_2RR [24–26]. Our research group has focused on tuning the selectivity of HFGDE by introducing different metal catalysts. For example, by adjusting the electrodeposition duration on Cu HF, the valence states of Sn were tuned, achieving a formate Faradaic efficiency exceeding 80 % in Sn-Cu HF [27]. Furthermore, uniform nanosheet-structured 2D bismuth catalysts were successfully grown on the surface of Cu HF, and the resulting electrode [26] outperformed the bulk bismuth on the Cu HF electrode, achieving over 5 times electrochemical surface area (ECSA) and 6 times catalyst activity in terms of formate production. In another contribution, 2D zinc nanosheets with adjustable Zn(101)/Zn(002) ratios were electrodeposited on the outer surface of Cu HF for syngas production [24]. Although the deposition of nano-electrocatalyst improved the CO_2RR activity of Cu HFGDEs, the current densities were still relatively low (around 100 mA/cm^2) by using low concentrations of electrolytes (e.g., 0.5 M $KHCO_3$). The limited current density is probably due to the relatively poor CO_2 distribution from the inhomogeneous pore geometry of HFGDEs, resulting in poor reaction kinetics and competing HER. However, tuning the pore structure of HFGDE requires balancing multiple parameters of the fabrication process, such as the ratio between polymer binders and metal powders, metal powder type/sizes, and sintering temperature/duration. Therefore, a post-treatment strategy is of great importance to modulate the electrode wettability, achieving more uniform CO_2 delivery, higher current density, and better CO_2RR activity.

Herein, we develop a facile strategy to enhance CO_2 distribution and optimize the triple-phase boundary formation by adjusting the wettability of HFGDEs. To reduce pore blockage and enhance pore utilization for gas diffusion, incorporation of a hydrophobic agent (e.g., PTFE) was carried out via infiltration-melting route, leading to a reduced pore capillary pressure and enhanced CO_2 distribution in the pristine 2D Zn nanosheets deposited Cu hollow fiber (named as P-HFGDE). The enhanced CO_2-distributed HFGDE with a 5 wt% concentration of PTFE water solution treatment (named ECD-HFGDE-x, x=PTFE concentration) exhibited improved Faradaic efficiency for CO production as the optimized electrode wettability could reduce the number of flooded pores and enhance the CO_2 distribution. The significant decrease in water flooding (fluorescent area), pressure drop, and enhancement in CO_2 bubbling confirmed the improvement of CO_2 distribution on the ECD-HFGDE-5 electrode, leading to a ~39 % increase in partial current density (PCD) of CO than the P-HFGDE. The CO_2RR performance of ECD-HFGDE-5 has also been investigated in non-GDE mode, where the CO_2 is directly bubbled into the electrolytes, only achieving a quarter of PCD of CO than the electrode performed in GDE mode. Lastly, the stability of ECD-HFGDE-5 was investigated, achieving around 4 times higher stability than the P-HFGDE. These experimental results indicate that the ECD-HFGDE-5 with enhanced CO_2 distribution could optimize the formation of triple-phase boundaries and promote the CO_2RR activity.

2. Experimental method

Chemicals, materials, and the fabrication of Cu hollow fiber are provided in Supporting Information.

2.1. The preparation of enhanced CO_2-distributed HFGDEs

The deposition of zinc nanosheets on Cu HFGDE was carried out using a similar method described in the previous report [24]. Briefly, the Cu hollow fiber was first submerged into a mixed electrolyte containing 0.6 M $ZnSO_4$ and 0.1 M $(NH_4)_2SO_4$. Then, a potential of −1.5 V (vs. Ag/AgCl) was applied on a potentiostat for 1 s on and 3 s off, for a total of 100 cycles. Subsequently, the samples were rinsed with deionized water multiple times before drying with N_2. The decoration of PTFE on the P-HFGDE was achieved by immersing the related electrodes into different concentrations of PTFE (5 wt%, 10 wt%, and 20 wt%) water solutions for several seconds, and obtained electrodes were raised with deionized water and dried in a vacuum oven for 4 h, followed with a thermal treatment, calcinated at 350 ℃ in Ar for half an hour. The obtained hollow fiber samples were stored in the N_2 atmosphere before further tests.

2.2. Characterizations

Scanning electron microscopy (SEM, JOEL-7100 F) was used to measure the surface morphology and the diameters (wall thickness) of HFGDEs. The water contact of the HFGDE surface was measured by a customized sessile drop equipment, and 1 μL of DI water was dropped on the outer surface of the electrodes. A confocal laser scanning microscope (Zeiss LSM 900) was used to observe the fluorescent images of HFGDEs with different pre-treatment conditions. The nanostructures of zinc nanosheets were inspected by Field Emission Transmission Electron Microscope (FETEM, Hitachi HF 5000, Japan). The crystalline structures of the bulk phase HFGDEs were analyzed by X-ray diffraction (XRD, Bruker advanced X-ray diffractometer, Cu Kα (λ=1.5405Å) radiation source, Japan). X-ray photoelectron spectroscopy (XPS) was applied to analyze the surface valence state and surface compositions of the HFGDEs. XPS was conducted on a Kratos Axis ULTRA XPS with a monochromatic Al Kα radiation source (1486.6 eV) at 15 kV (10 mA) and a hemispherical electron energy analyzer (165 nm). CASA® software was used to analyze the XPS data, calibrated to the C 1 s signal at 284.4 eV as the reference. The functional group of PTFE was probed by FT-IR on a Spectrum 100 system equipped with an ATR detector from PerkinElmer.

2.3. Electrochemical measurements

The CO_2RR performances of HFGDEs were carried out in a homemade H-cell. The working electrode (HFGDE) was stuck into a ¼ copper tube via conductive silver epoxy, and the other end, along with joints, was sealed and covered with non-conductive and gas-tight epoxy, with an exposed length of 2 cm. The geometric area of ECD-HFGDE-5 is 1.04 cm^2 (S=πDoutL =π×1.66×0.1×2=1.04 cm^2, where S is the electrode area, Dout is the outer diameter of hollow fiber, and L is the length of hollow fiber). The geometric areas of HFGDEs were summarized in Table S1. An Ag/AgCl (3 M NaCl, BASi, USA) was used as a reference electrode, with a Pt sheet (3×3 cm^2) as the counter electrode. Nafion 117 Proton Exchange Membrane was used to separate the anode and cathode chambers. The potentials applied on the potentiostat (Autolab PGSTA302N with FRA32M) were converted to the reversible hydrogen electrode (RHE) scale via E (V vs. RHE) = E (V vs. Ag/AgCl) + 0.209 +0.0591 pH. The potential in this manuscript was used in the RHE scale without RS competence. The pH value for 3 M KCl was measured by a pH meter (TPS, WP-Plus), and the value is around 6.8 in CO_2-saturated 3 M KCl (with 0.1 M $KHCO_3$ as buffer) solution. Here, it should be noted the 3 M KCl solution mentioned in this manuscript added 0.1 M $KHCO_3$ as a

pH buffer. A 3 M KCl solution was used as catholyte and a 3 M KOH was applied to the anolyte. Before the test, the H-Cell was vacuumed and purged with 30 ml/min CO_2 for 30 min.

The stability test was performed in a home-built flow cell by peristaltic pumps to circulate electrolytes (3 M KOH or 3 M KCl) in the anodic or cathodic sections. Anode and cathode compartments had a volume of 54 ml, and two extra reservoir containers with a volume of 250 ml were used for catholyte and anolyte circulation with a flow of 20 ml/min, and CO_2 purging through the electrodes (30 ml/min). Samplings for liquid and gas were done once per hour. For each electrochemical test, the average of three times repeat is reported.

The calculation of dual-layer capacitance (Cdl), product quantification, calculation of CO_2 permeability, in-situ Raman microscopy, and computational fluid dynamic (CFD) calculations are provided in Supporting Information.

3. Results and discussion

3.1. Microstructure and morphology analysis

Fig. 1a presents the enhanced CO_2-distributed hollow fiber gas-diffusion electrode (ECD-HFGDE) design strategy, which mainly requires electrocatalyst deposition and decoration with a hydrophobic agent (e.g., PTFE). The tubular architecture of HFGDEs can be observed

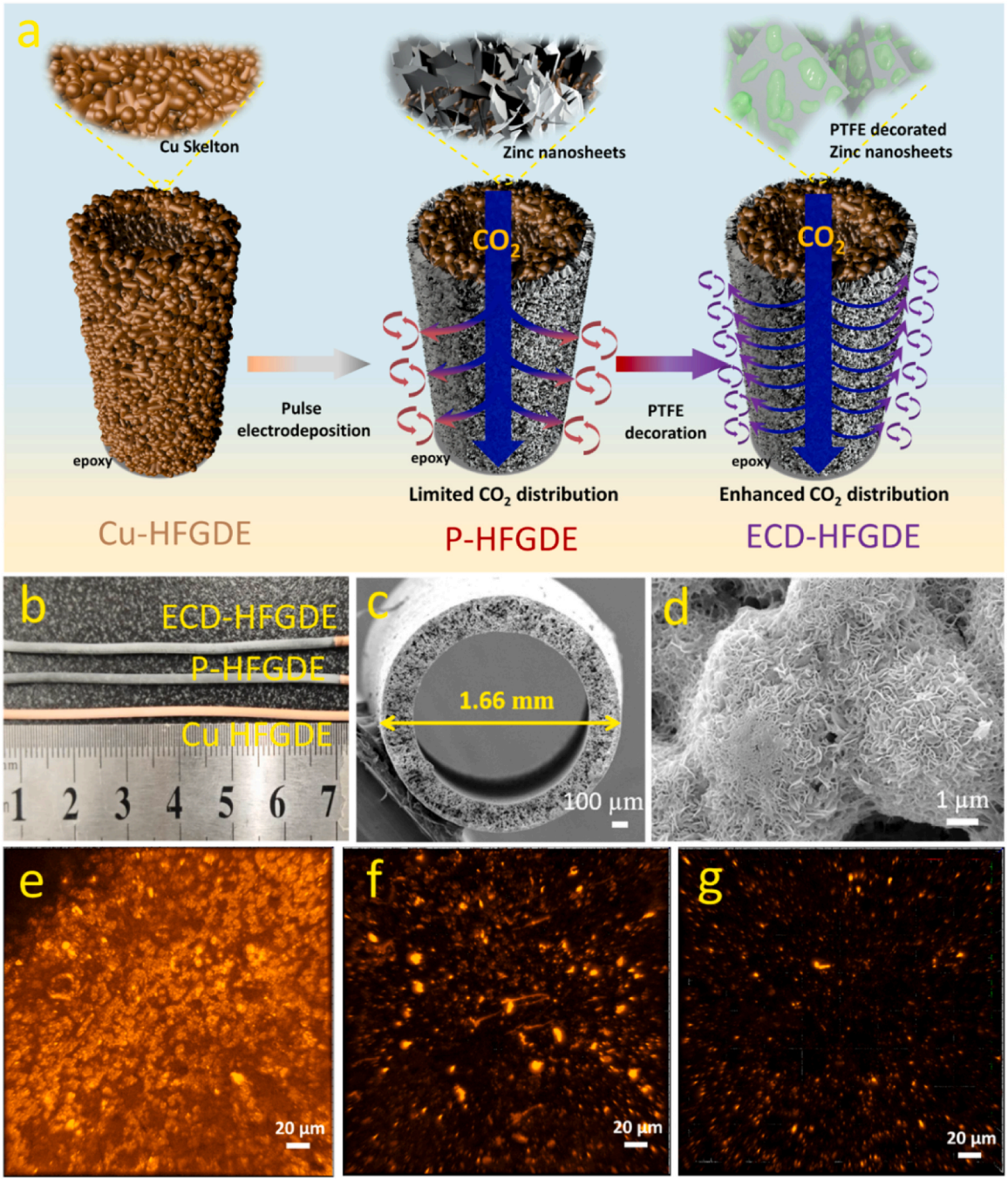

Fig. 1. **(a)** Schematic illustration of preparing enhanced CO_2 distributed HFGDE with PTFE decoration; **(b)** photo images of Cu HFGDE, P-HFGDE, and ECD-HFGDE; **(c)** cross-sectional SEM image of Cu-HFGDE; **(d)** SEM images of ECD-HFGDE-5; confocal fluorescent images of **(e)** P-HFGDE without gas flow through, **(f)** P-HFGDE, and **(g)** ECD-HFGDE-5 with 30 ml/min CO_2 flow through.

from Fig. 1b, and the lumen side of HFGDE can serve as a gas chamber for gas delivery, differing from planar diffusion electrodes. As an electron conductor and gas disperser, the copper hollow fiber was selected to deposit 2D zinc nanosheets through the pulse-electrodeposition technique, and zinc nanosheets can function as active sites for CO production. The porous structure and gas permeability of Cu HFGDE substrate are crucial for CO_2 distribution and to achieve high local CO_2 concentration near catalyst-electrolyte interfaces. The abundant micron pores of the hollow fiber walls were observed from the cross-sectional SEM images of Cu HFGDE substrates (Figs. 1c, S3a-3i). The diameter of applied copper hollow fiber was around 1.5–1.7 mm, with a wall thickness of around 200±20 μm (Figs. 1c, S3a-3i). The gas permeability of copper hollow fiber substrate was calculated by Eq. S3; the related value is around $2.94 \pm 0.04 \times 10^{+6}$ Barrer in the same range as the value ($4 \pm 0.05 \times 10^{+6}$ Barrer) reported in the reference [28], indicating a sufficient gas delivery capacity from the enriched micron porous structure.

The copper HFGDE substrate with a high surface-to-volume ratio can provide sufficient surface area to grow dense zinc nanosheets. The successful deposition of zinc nanosheets can be overserved from Fig. 1b, with the disappearance of copper color in the P-HFGDE, indicating a uniform coverage of zinc catalyst on the outer surface of Cu HFGDE. The SEM image of the P-HFGDE surface (Fig. S3j) also confirmed the dense 2D zinc nanosheets grown on the outer surface, and the thickness of the zinc nanosheet layer was around 1–2 μm observed from the cross-sectional SEM image (Fig. S3k). The gas permeability of P-HFGDE is around $2.78 \pm 0.03 \times 10^{+6}$ Barrer, slightly smaller than the value of Cu HFGDE substrate ($2.94 \pm 0.04 \times 10^{+6}$ Barrer), suggesting that the coverage of the zinc catalyst layer did not block the micron pores of hollow fiber and retains the outstanding permeability for gas transportation.

The decoration of polytetrafluoroethylene (PTFE) can enhance the CO_2 distribution on the HFGDE by introducing hydrophobicity and decreasing the capillary pressure inside the pore structures [29–32]. Herein, the ECD-HFGDEs were fabricated by immersing the P-HFGDE in 5 wt%, 10 wt%, and 20 wt% PTFE water solutions for several seconds, followed by a short-period thermal treatment in Argon at 350 ℃. The SEM images of the HFGDE surface before thermal treatment (Figs. S31-3n) revealed that PTFE nanoparticles covered the outer surface of the zinc nanosheets, and the coverage increased with the increase of PTFE loading. After thermal treatment, the zinc nanosheets were re-exposed with the PTFE nanoparticles melting and re-distributing on zinc nanosheets (Fig. 1d, S3o, and S3p). The distribution of PTFE on the ECD-HFGDE-5 was revealed by the energy dispersive spectroscopy (EDS) elements mapping images of the zinc nanosheet (Fig. S4), with the F element homogenously dispersed on the zinc nanosheet. It should be noted that the excessive amounts of PTFE could result in a thick PTFE layer covering the zinc nanosheets (Fig. S3p), leading to the reduction of zinc catalytic sites for the reaction. The wettability of HFGDEs was modulated by different PTFE loading, which was roughly estimated by the water contact angle. The hydrophilic surface of P-HFGDE revealed a 50° water contact angle (Fig. S5a), and the hydrophobicity of ECD-HFGDEs can be further improved by increasing PTFE loading. The improved hydrophobicity of ECD-HFGDE-5 can also be observed from the water-dropping test of photo images of P-HFGDE (Fig. S5b) and ECD-HFGDE-5 (Fig. S5c).

To illustrate the improved CO_2 distribution following PTFE decoration on the HFGDE, confocal laser scanning microscopy was applied to observe the fluorescent residue of HFGDE under various treatment conditions. The surface of hydrophilic P-HFGDE without CO_2 flow showed a complete fluorescent coating (Fig. 1e). Conversely, a notable reduction in fluorescent residue was seen on the P-HFGDE with a 30 ml/min CO_2 flow (Fig. 1f), suggesting that the gas flowing-through HFGDE could help mitigate the flooding issue. From Fig. 1g, S6a, and S6b, the fluorescent residue continuously decreased with increased PTFE loading of the HFGDE. Furthermore, the fluorescent wetted area was quantitatively analyzed for CO_2 distribution, and the value of ECD-HFGDE-5 dropped almost 66.7 % compared to that of the P-HFGDE under CO_2 flowing through, indicating the PTFE decoration results in homogeneous CO_2 distribution on the surface. The water penetration depth of the ECD-HFGDE-5 was observed from the confocal cross-sectional fluorescent image (Fig. S6c), exhibiting a smaller fluorescent residue depth than that of the P-HFGDE (Fig. S6d). These results indicated the improved CO_2 distribution on the ECD-HFGDE-5, as the decoration of PTFE could reduce the capillary pressure of the pores and reduce the number of flooded pores.

The crystal structure of the HFGDEs was investigated via X-ray diffraction (XRD), and the results are presented in Fig. 2a and 2b. The observation of strong background peak copper diffraction peaks (Fig. 2a) and catalytic zinc characteristic peaks of Zn (002) and Zn (001) on the HFGDEs (Fig. 2b) were in accordance with the previous report [24,25]. The decoration of PTFE in ECD-HFGDEs will not alter the zinc crystal facets compared to the P-HFGDE, as confirmed by the high-resolution scanning transmission electron microscopy (HR-STEM), the characteristic spacing of 0.260 nm of Zn (002) emerging in both P-HFGDE (Fig. S7) and ECD-HFGDE-5 (Fig. 2c) samples.

The high-resolution XPS was conducted to reveal the electronic states of elements (Zn, Cu, F, O) for HFGDEs and Figs. S8, S9, 2d, 2e, and 2f illustrated the XPS spectra of Cu 2p, Zn 2p, F 1s, and O 1s, respectively. The disappearance of the Cu 2p signal (932.5 eV) (Fig. S8) in P-HFGDE and ECD-HFGDEs (Fig. S9) indicated a relatively uniform zinc catalyst layer coverage on the outer surface of the Cu HFGDE substrate [24]. The XPS spectra of Zn $2p_{3/2}$ and Zn $2p_{1/2}$ peak for the HFGDEs were each deconvoluted into two separate peaks (Fig. 2d), and the relatively high binding energy peaks 1025.0 eV and 1048.0 eV are associated with the oxidized zinc (Zn^{2+}) state. In contrast, the relatively low binding energy peak at around 1022.2 eV and 1045.2 eV is associated with the metallic Zn (Zn^0 state) [24]. The ratios of different zinc states for HFGDEs were calculated in Table S2. The metallic Zn^0 state could be the dominant zinc catalytic site for the CO_2RR to CO, accounting for more than 75 %. The P-HFGDE possessed the highest ratio of metallic Zn^0 state, around 88.1 %, compared to that of ECD-HFGDEs. The Zn^{2+} ratio slightly increased with the increased PTFE loading, possibly attributed to the existence of the C-F bond from PTFE attracting the electrons of the Zn atom [33].

The F 1 s peak at around 689 eV detected in the ECD-HFGDEs corresponds to the C-F of PTFE, without observation of the F 1 s peak in the P-HFGDE (Fig. 2e). The Fourier-transform infrared spectroscopy (FTIR) results (Fig. S10) further confirmed the successful decoration of PTFE on ECD-HFGDEs, with the observation of two C-F bond vibration peaks at around 1148 and 1203 cm^{-1} [33], and the related peak signal increased with the increased PTFE loading. The detected O 1 s peaks of HFGDEs were divided into three different peaks at 531.6, 532.5, and 534.0 eV (Fig. 2f). The binding energy peak at 531.6 eV corresponds to the Zn-O species, and the peak at 532.5 eV is associated with the Zn-OH species. The high binding energy peak at 534.0 eV is usually attributed to the adsorbed water on the electrode surface [25].

3.2. *Optimal PTFE loading for improved triple-phase boundary formation and CO_2 distribution*

The improvement in CO_2RR activity demands optimization of water management in GDE to reduce the distance of the CO_2 diffusion pathway in the double-phase (liquid-solid) boundaries or increase the formation of triple-phase (gas-liquid-solid) boundaries. The liquid electrolytes driven by capillary action will preferentially pass through the pores with low capillary pressure resistance. Thus, the small hydrophilic and large hydrophilic pores of GDEs are most likely to be flooded [34,35]. To reduce the formation of flooded pores, the HFGDE configuration provides opportunities to overcome capillary pressure by regulating the gas flow rates. However, it required a relatively uniform pore size distribution on HFGDE. Otherwise, the relatively inhomogeneous pore size

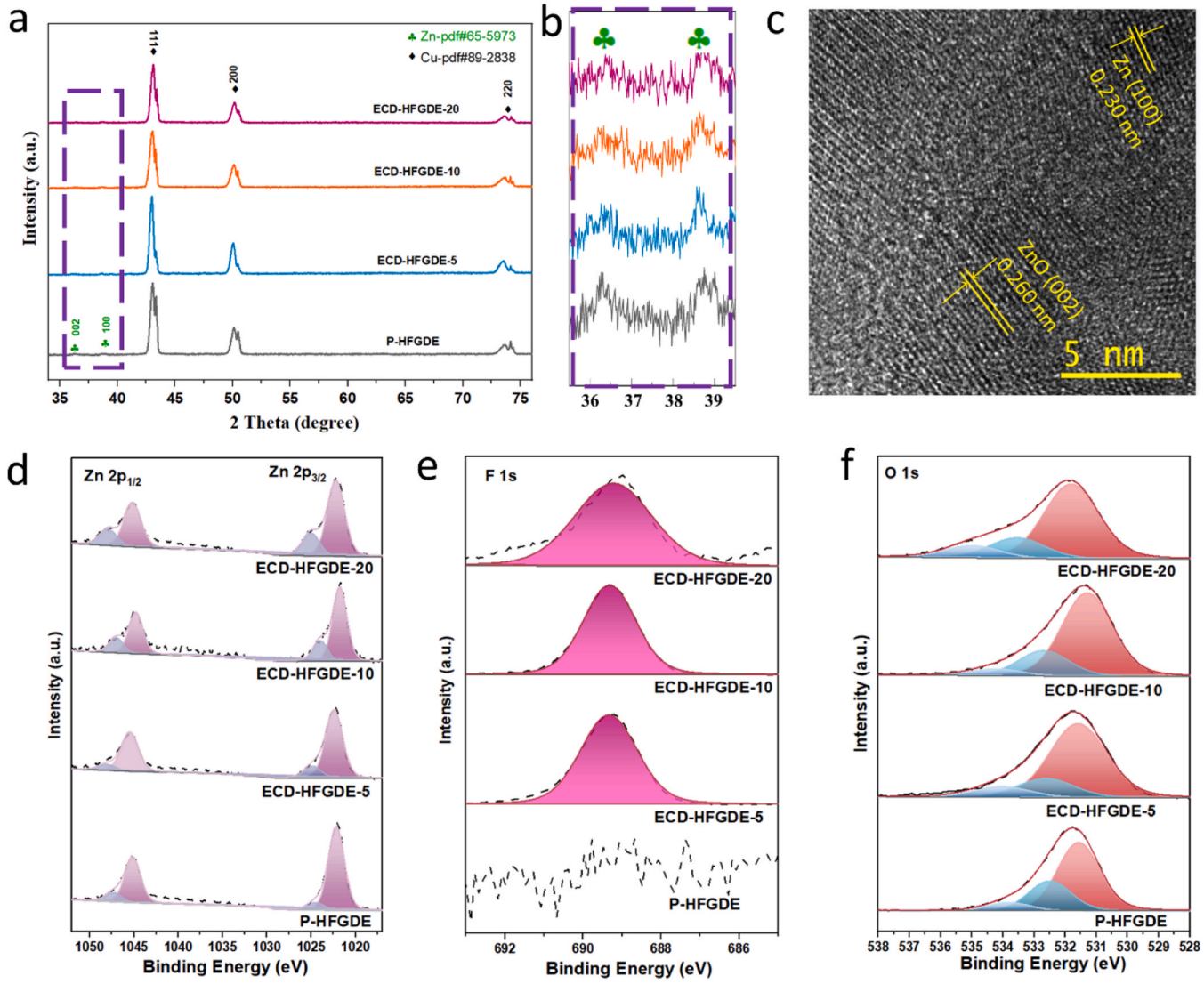

Fig. 2. **(a)** XRD patterns, and **(b)** magnification XRD patterns (35–40) of HFGDEs; **(c)** STEM image of the ECD-HFGDE-5 sample; XPS spectra of **(d)** Zn $2p_{3/2}$ **(e)**, F 1 s, and **(f)** O 1 s composition of HFGDEs.

distribution will lead to a low pore utilization for gas diffusion, resulting in limited CO_2RR activity.

The decoration of PTFE could also reduce the formation of flooded pores (Fig. 3a), where the gas transportation channels are eliminated, indicating high mass transfer resistances for gas transportation [34]. The CO_2 local concentration near the flooded pores is limited due to the long diffusion path (over around 50 μm) [15,34] and low CO_2 aqueous solubility (33 mM) for the dissolved CO_2 transport from the bulk electrolyte to the catalytic sites (Fig. 3b). The optimized PTFE loading can increase the formation of partially wetted pores (Fig. 3c), where a certain number of gas transfer channels are retained around the PTFE with sufficient electrolytes on catalyst layer [30,31]. Thus, maximize the chances of triple-phase (CO_2-electrolyte-catalyst) interface formation, where the CO_2RR is more likely to happen with abundant CO_2 supply with a short diffusion path of around 50 nm (Fig. 3d). However, excessive amounts of PTFE loading could lead to the formation of dry pores (Fig. 3e), which is an ideal situation with PTFE film fully covering the whole active sites of the electrode. The coverage of PTFE film will lead to poor CO_2RR performance due to a lack of proton supply from the electrolyte and disruption of the electrolyte-catalyst interface. (Fig. 3f).

Furthermore, the decoration of PTFE on HFGDEs enables wettability manipulation to regulate the capillary pressure and improve the CO_2 distribution. The different PTFE loading on HFGDEs alter the wettability on the HFGDE surface (Fig. S5a), and a significant reduction of pressure drop was observed in Fig. 3g. The P-HFGDE exhibited the highest pressure drop of 6.4 psi when a 30 ml/min CO_2 flow was applied, sharply dropping to 1.8 psi for ECD-HFGDE-5. This around 61 % decrease in the pressure drop indicated a significant decrease of capillary pressure and improvement in the pore utilization for CO_2 diffusion. Compared to the hydrophilic P-HFGDE, the CO_2 gas bubbling on the outer surface of the ECD-HFGDE-5 (Fig. 3h) significantly improved, suggesting enhanced CO_2 distribution with PTFE decoration.

3.3. CO_2RR performance of HFGDEs

The HFGDEs with different PTFE loading were performed in a customized H-Cell to investigate the CO_2RR activity. From the linear sweep voltammetry (LSV) of HFGDEs (Fig. S11), the highest current density was observed from the P-HFGDE, compared to ECD-HFGDEs with surface PTFE decoration. The increased PTFE loading led to the decreased current density for the ECD-HFGDEs due to the reduced electrolytes wetting area. The dual-layer capacitance (Cdl) of the HFGDEs was conducted via cyclic voltammetry (CV) scanning at different scan rates (Fig. S12), shown in Fig. 4a. The P-HFGDE possessed

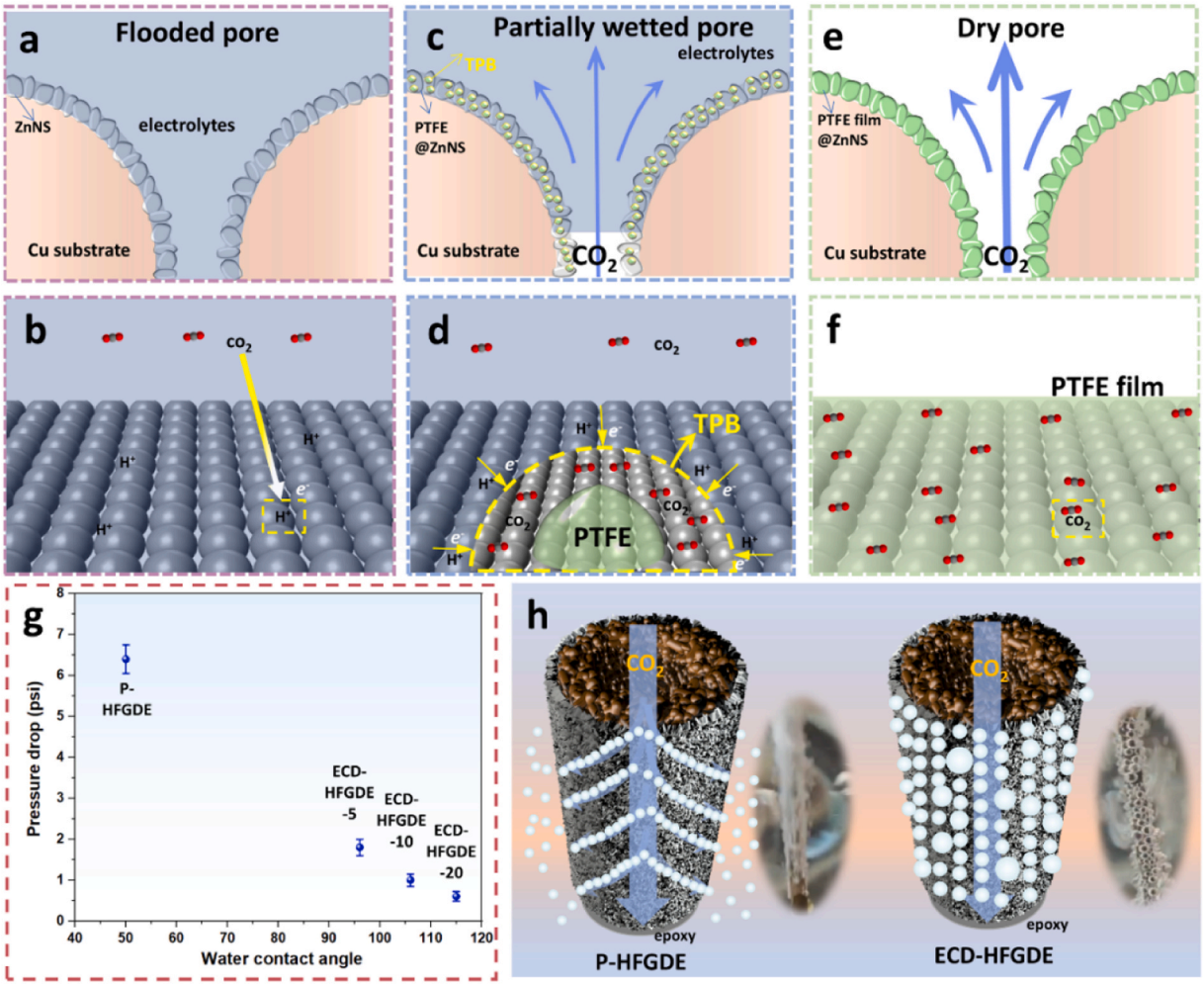

Fig. 3. Schematic of the **(a)** flooded pores and **(b)** CO_2 transportation and CO_2RR with dissolved CO_2; **(c)** partially wetted pores and **(d)** CO_2 transportation and CO_2RR in optimized triple-phase boundaries; **(e)** dry pores and **(f)** CO_2RR in gas-catalyst interfaces; **(g)** pressure drop over HFGDEs with different contact angles with a 30 ml/min CO_2 flowing through; **(h)** schematic and inserted photo images of CO_2 distribution in P-HFGDE (left) and ECD-HFGDE-5 (right).

the highest Cdl of 83.7 mF/cm^2, which is more than 6 times higher than 12.6 mF/cm^2 from the ECD-HFGDE-20 electrode. In addition, the Cdl value of ECD-HFGDE-5 is 66.2 mF/cm^2, 51.8 mF/cm^2 for the ECD-HFGDE-10 electrode, indicating the decreased ECSA (active sites) with increased loading of PTFE. The decrease in current density could also be attributed to the increased charge-transfer resistance after decorating non-conductive PTFE [36]. The kinetics of electron transfer for HFGDEs was evaluated by the electrochemical impedance spectroscopy (EIS) measurement at −0.8 V (vs. RHE) in Fig. 4b, and the ECD-HFGDE-20 exhibited the largest charge transfer resistance due to excessive non-conductive PTFE covering catalyst surface (Fig. S3p) and the increased number of dry pores (Fig. 3e).

The CO_2 local concentration near catalytic sites is critical for suppressing HER at high overpotentials or current densities [37,38]. Although the hydrophilic P-HFGDE exhibited the largest ECSA and the smallest charge transfer resistance, it exhibited poor CO selectivity (Fig. 4c), especially at high overpotentials, where flooding is more likely to happen due to electrowetting. This could cause flooding in the pores of P-HFGDE (Fig. 3a) where the competitive HER is dominant due to the fast electron transfer (Fig. 3b). The optimization of PTFE loading could enhance the CO_2 distribution, providing sufficient CO_2 near triple-phase boundaries and suppress HER. The ECD-HFGDE-5 with optimized PTFE loading exhibited a high Faradaic efficiency (Fig. 4c) of over 80 % for CO at a high overpotential range from −1 to −1.3 V (vs. RHE), and it reached the highest CO Faradaic efficiency of 85.4 % at −1.1 V (vs. RHE). The ECD-HFGDE-5 with partially wetted pores (Fig. 3c) also exhibited the highest partial current density of CO (Fig. 4d), reaching 251.8 mA/cm^2 at −1.3 V (vs. RHE) with a CO production rate (Fig. S13) of 4696.9 μmol/h•cm^2. The improved CO_2RR activity for ECD-HFGDE-5 is due to the enhanced CO_2 gas distribution and the optimized triple-phase boundaries for the reaction. The ECD-HFGDE-20 closed to the dry pore situation (Fig. 3e) exhibited poor CO_2RR performance and achieved only 1/3 partial current density of CO, compared to that of the ECD-HFGDE-5 electrode.

For CO_2RR to CO with zinc-based catalysts [39,40], CO_2 is firstly adsorbed on the zinc catalysts surface, being reduced to CO_2* via one electron contributing from the electrochemical process and then to COOH* intermediates via a proton transfer step. Most of the COOH* intermediates are reduced with a proton and an electron to CO* that desorbs from zinc catalyst to form the main product CO. To illustrate the underlying mechanism of CO production, the Tafel slope (Fig. 4e) was used to analyze the CO_2 to CO conversion kinetics. The Tafel slop with a value of 118 mV/dec indicates the rate-limiting step during CO_2RR is the initial one electron transfer step. The Tafel slope values of HFGDEs were all above 118 mV/dec, suggesting that the reaction rate-determining step is the CO_2 activation to CO_2* [9]. The ECD-HFGDE-5 exhibited the smallest Tafel slope value of 166 mV/dec, suggesting the fast reaction kinetics owing to the well-distribution of CO_2 gas. The hydrophilic P-HFGDE electrode showed high Tafel values at both low and high potentials, indicating its low CO_2RR activity

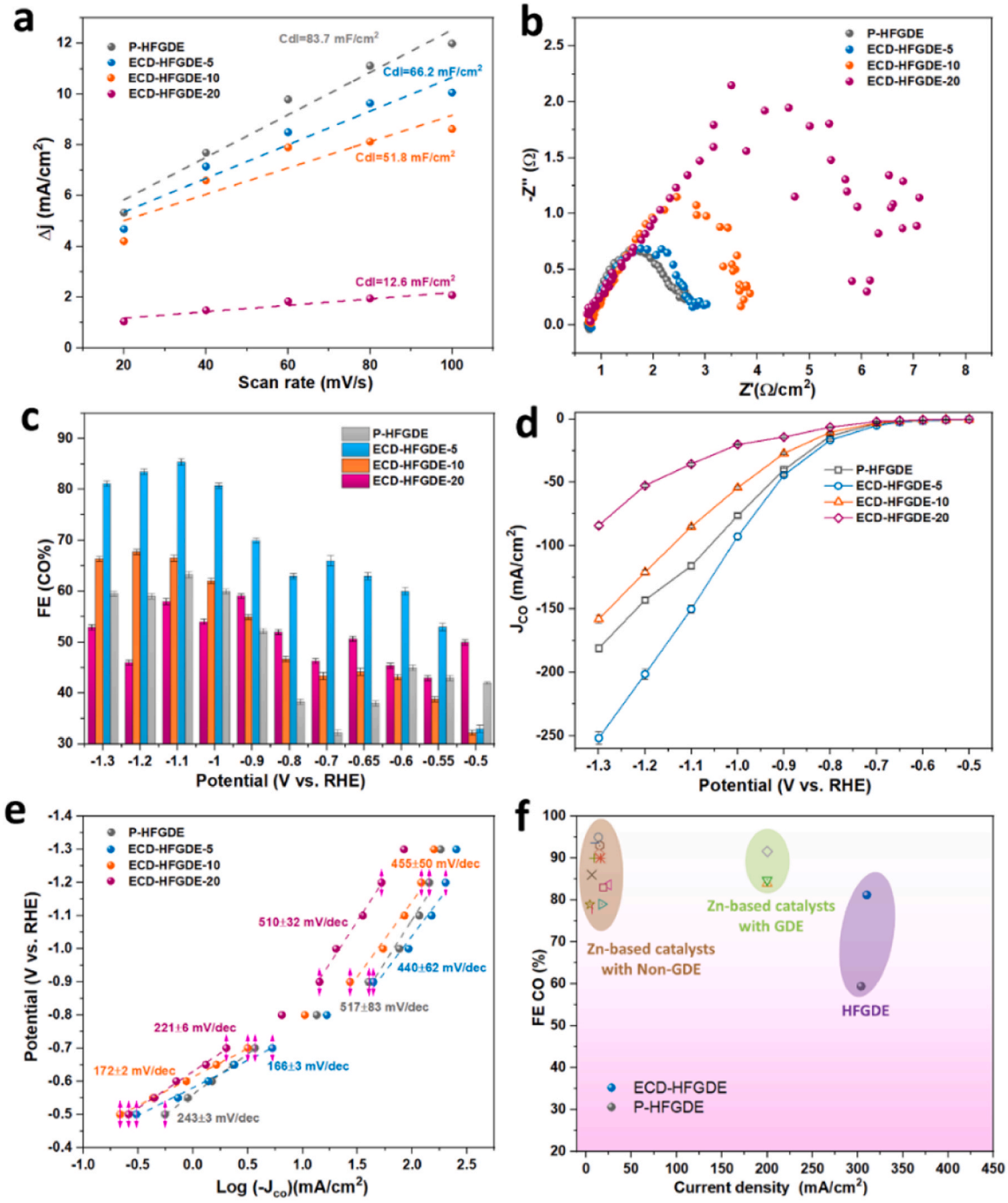

Fig. 4. **(a)** Dual-layer capacitance (Cdl) values over HFGDEs; **(b)** Nyquist plots to evaluate electron resistance behavior of HFGDEs; **(c)** Faradaic efficiency of CO for HFGDEs; **(d)** partial current density of CO for HFGDEs; **(e)** Tafel plots over HFGDEs to evaluate reaction kinetics; **(f)** comparison of zinc-based electrocatalyst with conventional planar electrodes performed in H-Cell, with GDE performed in flow-type cells; P-HFGDE, and ECD-HFGDE-5 electrodes performed in H-Cell.

towards CO production. Here, although the ECD-HFGDE-20 electrode indicated a higher FE of CO than the ECD-HFGDE-10 electrode, its low current densities due to excessive PTFE decoration resulted in a lower partial current density with a lower Tafel slope. The oxidative LSV (Fig. S14) was also conducted for HFGDEs in N_2-saturated 0.1 M potassium hydroxide to evaluate the binding ability of CO_2*. This method has been applied in several studies on CO_2RR with different electrocatalysts such as Sn [41], Bi [42], Ag [43], and Zn [33], and the more negative potential required for OH^- adsorption suggested the high binding energy for CO_2*. The potential for the OH^- adsorption peak of ECD-HFGDE-5 was more negative than that of P-HFGDE, suggesting a stronger adsorption ability on the ECD-HFGDE-5 to facilitate the CO_2 activation step.

The potential-related in-situ Raman spectroscopy was applied to further explore the mechanism of CO_2RR over P-HFGDE and ECD-HFGDE-5. As revealed by Fig. S15, two typical Raman peaks were located at around 410 cm^{-1} and 528 cm^{-1}, corresponding to adsorbed *COOH and *COO^- intermediates on the electrode surface. These are key intermediates for the electrochemical conversion of CO_2 to CO via a concerted proton-electron transfer (CPET) step. The peak intensity of *COOH and *COO^- increased when moving to more negative potentials, implying more intermediates adsorbed on the electrode surface, which

aligns with the CO_2RR activity trend. It should be noted that the peak intensity of *COOH and *COO^- of ECD-HFGDE-5 were higher than that of P-HFGDE, indicating enhanced binding strength for *COOH and *COO^- intermediates on the electrode surface, which is in line with the oxidative LSV results. These Raman results can provide an in-situ evidence that PTFE-decorated zinc nanosheets could enhance the CO_2 activation kinetics to facilitate CO_2 conversion at lower current densities.

Although the number of active sites and the intrinsic activity of advanced electrocatalysts is the key to maintaining high selectivity for CO production under low current density, the CO_2 mass transportation and CO_2 availability become crucial when applying high current density [35]. The fast electron transfer through the electrode at high current density will lead to an intense tug of war between CO_2 and water. The pore utilization and CO_2 diffusion of HFGDEs are crucial to supress competitive HER. To gain insights into the pore utilization and CO_2 distribution over P-HFGDE and ECD-HFGDE-5 electrodes, the Laminar flow and stationary study were used for the computational fluid dynamic (CFD) modeling (Fig. S16). The color gradient from red to blue represents the decrease of CO_2 velocity. The definition of flooded pores (no CO_2 flush through) and opened pores (CO_2 flush through) numbers were based on the confocal laser fluorescent microscopy data. The simulation results illustrated that CO_2 gas continuously rushed through the micron-pore structures of the HFGDE and flushed into the electrolyte, which will provide sufficient CO_2 near the catalysts-electrolytes interfaces. In addition, the turbulent CO_2 gas surrounding opened pores could facilitate the local mixing of reactants, resulting in an improved mass transfer and reaction kinetics. However, in those flooded pores, the CO_2 delivered from the bulk electrolytes with large mass transportation resistance. Therefore, the ECD-HFGDE-5 with enhanced pore utilization numbers could maximize the formation of triple-phase boundaries to improve the electrochemical conversion of CO_2, especially at high current densities.

At last, we have summarized the CO_2RR performance of zinc-based electrocatalysts with conventional planar electrodes performed in H-Cells [7–9,11,12,39,44–49], Zn-based GDE performed in flow-type cells [8,12,50], and HFGDEs performed in H-Cells in Table S3 and Fig. 4f. The Zn-based electrocatalyst with planar electrodes tested in H-Cells exhibited high Faradic efficiency over 80 % but suffered low current density due to the deprived supply of CO_2 near the catalytic sites. The Zn-based GDE incorporated with flow cells can operate at a current density of 200 mA/cm^2 and achieve more than 80 % Faradaic efficiency for CO by employing alkaline electrolytes or higher concentrations of neutral electrolytes (e.g., $KHCO_3$). The significant improvement towards current density in Zn-based GDE is because of the significantly shorted CO_2 diffusion path, as the diffusion path in non-GDE condition from bulk electrolytes to electrodes is about 50 μm, while the diffusion path in GDE condition from the CO_2 gas phase to the electrode surface is only about 50 nm [15,16]. The ECD-HFGDE-5 achieved a high current density (>300 mA/cm^2) and a decent Faradaic efficiency (>80 %) for CO production. Here, it should be noted that the outstanding CO_2RR performance by flow-through HFGDEs can even achieved in the H-Cell testing.

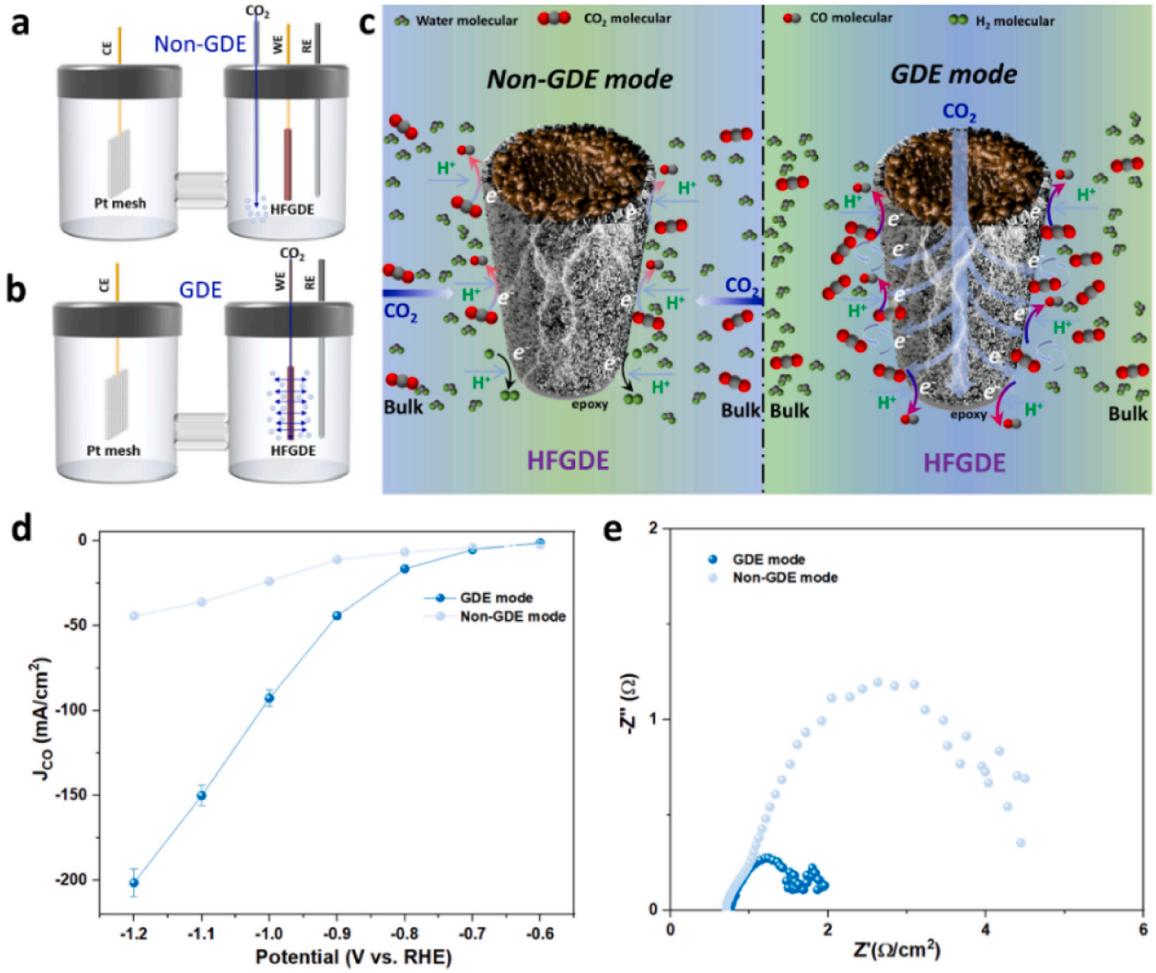

Fig. 5. **(a)** CO_2 delivery with non-GDE condition in H-Cell; **(b)** CO_2 delivery with GDE condition in H-Cell; **(c)** Schematic illustrations of CO_2RR performance over HFGDEs in non-GDE condition and GDE condition; **(d)** partial current density of CO over ECD-HFGDE-5 in non-GDE and GDE condition; **(e)** EIS Nyquist plots over ECD-HFGDE-5 in non-GDE and GDE condition at −1 V (vs. RHE).

3.4. CO_2RR performance of HFGDE in non-GDE and GDE mode

To further emphasize the exceptional CO_2RR performance from flow-through HFGDE operation, we also explored the HFGDEs in non-GDE mode (Figs. S17a-e). The gas delivery configuration of non-GDE mode is presented in Fig. 5a, where CO_2 gas was directly bubbled into electrolytes. In GDE mode (Fig. 5b), the end side of hollow fiber electrodes was sealed by epoxy, and the CO_2 gas was fed from the lumen side and pushed through the micron pores of hollow fiber walls, reaching the outer surface of HFGDEs. From Fig. 5c, in the non-GDE mode, the CO_2 gas was dissolved in bulk electrolytes and transported to active sites with a long-diffusion path, resulting in increased mass transport resistance and limited CO_2 local concentration near the active sites. However, in the GDE mode, the continuous CO_2 flow accumulates on the inner side of the hollow fiber and reaches a certain pressure to overcome the capillary pressure, providing sufficient CO_2 at triple-phase interfaces.

In non-GDE mode, although the PTFE decoration could deteriorate the charge transfer resistance of the electrode (Fig. S17b), an optimized PTFE loading can facilitate the formation of triple-phase interfaces to suppress HER [33], promoting CO_2RR to CO production. The ECD-HFGDE-5 electrode demonstrated a stable Faradaic efficiency of CO above 70 % over a wide potential range from −0.6 to −1.2 V (vs. RHE), as shown in Fig. S17c. In contrast, the hydrophilic P-HFGDE in the non-GDE mode with the flooded pores (Fig. 3a), exhibited poor CO selectivity (Fig. S17c), especially at high overpotentials due to the formation of flooded pores by electrowetting, causing insufficient CO_2

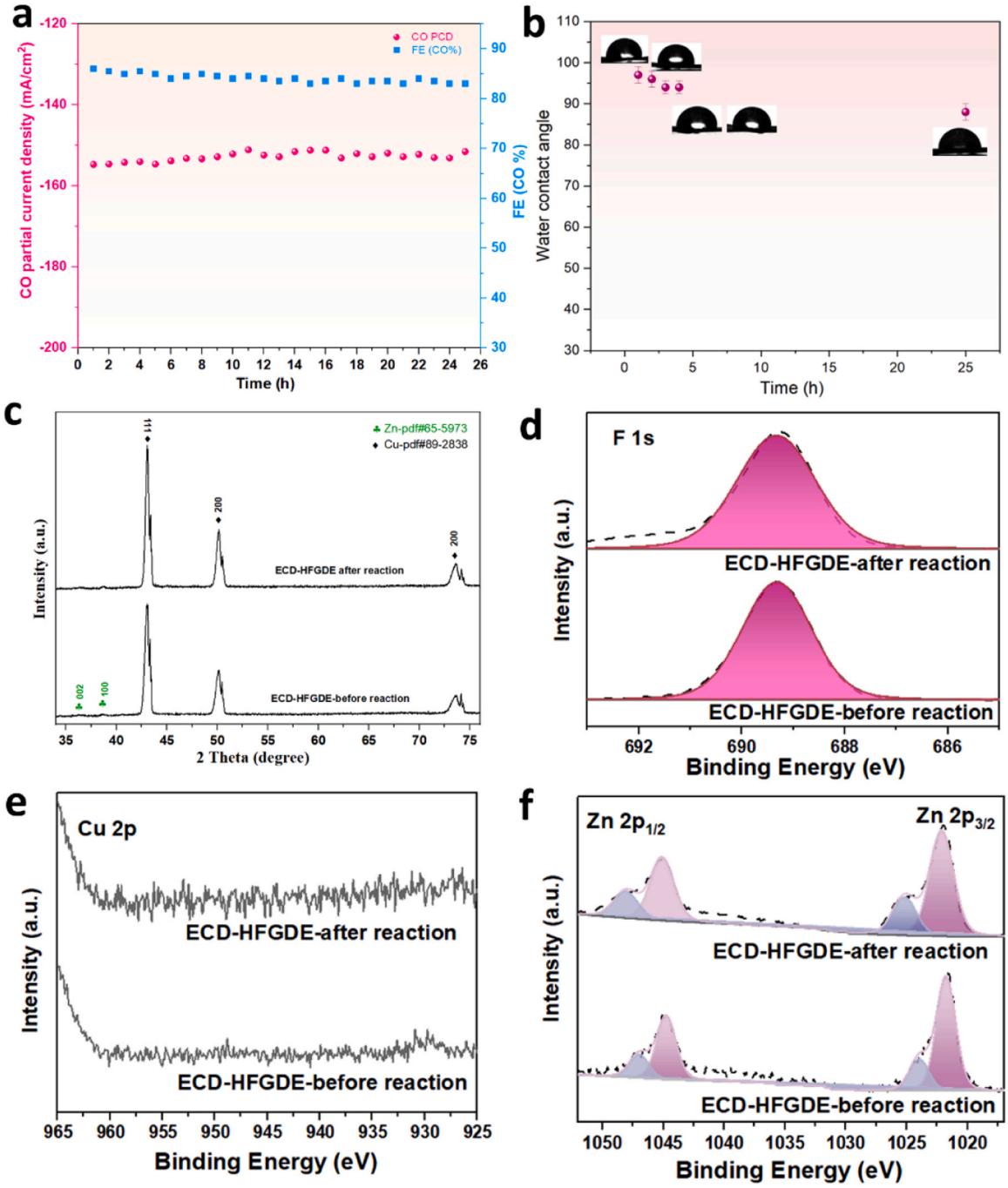

Fig. 6. **(a)** long-term operation of ECD-HFGDE-5 in flow-cell at −1.1 V (vs. RHE); **(b)** water contact angles of ECD-HFGDE-5 after 1 h, 2 h, 3 h, 4 h, and 25 h stability test; **(c)** XRD of ECD-HFGDE-5 before and after stability test; XPS spectra of **(d)** F 1 s, (e) Cu2p, and (f) Zn 2p over ECD-HFGDE-5 before and after stability test.

availability near the electrode surface for CO_2RR. The ECD-HFGDE-5 also showed the highest partial current of CO (Fig. S17d) and the CO production rate (Fig. S17e) over a potential range from −0.8 to −1.1 V (vs. RHE).

The CO_2RR activity of ECD-HFGDE-5 in GDE mode exhibited significant enhancement in the CO partial current density (150.1 mA/cm^2), which is more than 4 times higher than that in the non-GDE mode (36.2 mA/cm^2), as seen in Fig. 5d. As revealed by the electrochemical impedance spectroscopy (EIS) test of ECD-HFGDE-5 at −1 V (vs. RHE), the ECD-HFGDE-5 in the non-GDE mode exhibited a much higher charge transfer resistance of 3.7 (Ω/cm^2), which is more than 3 times higher than that of GDE mode (1.15 Ω/cm^2) (Fig. 5e). This suggests that the fast electron transfer and improved reaction kinetics occur in GDE mode due to the sufficient CO_2 supply and maximized triple-phase boundaries from HFGDE configuration.

3.5. The stability of HFGDEs

The stability of the HFGDEs was evaluated in a customized flow cell (Fig. S18) due to a stable environment (such as pH) favoring the CO_2RR. The CO_2 flow rate was kept at 30 ml/min, and the catholyte (3 M KCl) as well as anolyte (3 M KOH) were circulated at 20 ml/min. The stability test of the ECD-HFGDE-5 electrode was performed at −1.1 (V vs. RHE), which is the potential for the highest FE of CO (85.4 %), performed in H-Cell. In certain scenarios of zinc catalyst degradation [5,51,52], the catalysts may undergo oxidation in a high pH environment and dissolve in the electrolytes. In addition, the zinc species can be detached from the substrates due to the rapid reaction rate of HER at high current densities. The improved CO_2 distribution on the ECD-HFGE-5 electrode could not only suppress HER but also alleviate the degradation of zinc catalysts. The ECD-HFGDE-5 electrode performed a stable partial current density for CO at around 152 mA/cm^2, with a CO Faradaic efficiency fluctuating around 83 % at −1.1 V (vs. RHE) over 25 h (Fig. 6a). The water contact angle of ECD-HFGDE-5 (Fig. 6b) slightly dropped to 88° after 25 h stability test, suggesting the retention of hydrophobicity due to PTFE surface decoration. From the SEM image (Fig. S19a), the intact zinc nanosheet structure could still be observed after the stability test. The diffraction peaks (Fig. 6c) Zn (002) and Zn (101) at 36.3° and 36.9° indicated the retaining of zinc catalysts on the surface of the ECD-HFGDE-5 electrode after the stability test. The two C-F bond vibration peaks at around 1148 and 1203 cm^{-1} were observed from FTIR (Fig. S19b), and a strong F 1 s at 689 eV (Fig. 6d) can also be detected after the stability test, indicating the retaining of PTFE on the zinc catalyst layer for ECD-HFGDE-5 electrode. The absence of a Cu 2p peak (Fig. 6e) at 932.4 eV can also indicate the retention of the zinc catalyst layer covering the ECD-HFGDE-5 electrode. After reaction, there was no significant change regarding the XPS spectra of the Zn $2p_{3/2}$ and Zn $2p_{1/2}$ peaks (Fig. 6 g) of the ECD-HFGDE-5. The ratio of the Zn^0 state still accounts for 72 % (Table S2), suggesting that optimized PTFE decoration can stabilize zinc catalytic states.

In contrast, the CO Faradic efficiency of P-HFGDE dropped significantly from 62 % to 44 % after 8 h of operation, and an increase of competitive HER from 37 % to 57 % was observed from Figs. S20a, b. The water contact angle (Fig. S20c) of the P-HFGDE electrode after stability decreased to 46°, indicating the increased hydrophilicity that could lead to the formation of more flooded pores. The SEM image (Fig. S20d) of the P-HFGDE electrode showed the disruption of the zinc nanosheet structure and the formation of large particle species. The XPS spectra of Zn 2p (Fig. S20e) peak of the P-HFGDE exhibited a significant change as the percentage of Zn^0 reduced from 85.5 % to 28 % (Table S2), suggesting a large percentage of Zn^{2+} species formed during the reaction. In addition, the appearance of the Cu 2p peak at 932.5 eV (Fig. S20f) in P-HFGDE after stability test indicated the exposure of the Cu substrate due to the potential dissolution of Zn^{2+} species into electrolytes. The formation of Zn^{2+} species and salt precipitation at flooded pores, caused by high local pH, could potentially block the pore structures of HFGDE, leading to decreased stability [52]. A previous study [51] also observed the detachment of electrocatalysts from the substrate with a high hydrogen evolution rate, and this could also occur in flooded pores due to the rapid electron transfer at high current densities. Therefore, to enhance the durability of the electrocatalyst and extend the stability of the HFGDEs, it is essential to improve the CO_2 distribution of the HFGDEs and reduce the formation of flooded pores. This study demonstrates the promise to unlock the potential of HFGDE to improve its gas distribution and create more triple-phase interfaces to promote their reaction kinetics and the stability of electrocatalysts and electrodes.

4. Conclusion

In this study, to mitigate flooding and improve pore utilization for CO_2 diffusion, we developed an enhanced CO_2-distributed HFGDE by optimized PTFE decoration to create triple-phase boundaries for the electrochemical conversion of CO_2 to CO. The improved CO_2 distribution on the ECD-HFGDE-5 electrode has been confirmed by the reduced fluorescent area (water surface coverage), decreased lumen side pressure drop, and enhanced CO_2 bubbling. The ECD-HFGDE-5 achieved the highest CO partial current density of 251.8 mA/cm^2 and CO product rate of 4696.9 μmol/h•cm^2, owing to the enhanced CO_2 distribution and optimized triple-phase interfaces. The ECD-HFGDE-5 in GDE mode also achieved more than 4 times higher CO partial current density than this electrode in non-GDE mode, where the CO_2 is directly fed into the electrolytes, indicating the importance of the HFGDE configuration to deliver sufficient CO_2 near triple-phase interfaces. In addition, the stability of ECD-HFGDE-5 has improved more than 4 times than the hydrophilic P-HFGDE. The PTFE decoration on ECD-HFGDE-5 improved CO_2 distribution, reducing flooded pores and suppressing HER, thus mitigating Zn^{2+} species formation and alleviating the potential detachment of zinc species. This study showcased the promise of applying enhanced CO_2-distributed HFGDEs to facilitate the electrochemical conversion of CO_2 at high concentrations of electrolytes and high current density.

CRediT authorship contribution statement

Guoliang Chen: Conceptualization, Data curation, Investigation, Formal analysis, Validation, Writing-origin draft, Writing- review & editing. **Lei Ge**: Conceptualization, Methodology, Supervision, Validation, Funding acquisition, Resource, Writing- review & editing. **Beibei Ma**: Data curation, Investigation. **Yizhu Kuang**: Data curation, Investigation. **Hesamoddin Rabiee**: Investigation, Formal analysis, Methodology, Funding acquisition, Validation, Writing- review & editing. **Fatereh Dorosti**: Investigation, Formal analysis. **Ashok Kumar Nanjundan**: Validation, Writing- review & editing. **Zhonghua Zhu**: Project administration, Resource, Writing- review & editing. **Hao Wang**: Project administration, Funding acquisition, Validation, Methodology, Supervision, Resource, Writing- review & editing.

Declaration of Competing Interest

The authors declare that they have no known competing financial interests or personal relationships that could have appeared to influence the work reported in this paper.

Acknowledgements

We acknowledge financial support from the ARC Future Fellowship (FT220100166), Discovery project (DP190101782) and Centre of Excellence for Green Electrochemical Transformation of Carbon Dioxide (CE230100017). We acknowledge the UniSQ 2022 Capacity Building Grant and SNSF Swiss Postdoctoral Fellowship (217305) awarded to Dr Hesamoddin Rabiee.

Appendix A. Supporting information

Supplementary data associated with this article can be found in the online version at doi:10.1016/j.apcatb.2024.124803.

Data Availability

Data will be made available on request.

References

[1] J.E. Huang, F. Li, A. Ozden, A. Sedighian Rasouli, F.P. García de Arquer, S. Liu, S. Zhang, M. Luo, X. Wang, Y. Lum, CO_2 electrolysis to multicarbon products in strong acid, Science 372 (2021) 1074–1078.

[2] F.P. García de Arquer, C.-T. Dinh, A. Ozden, J. Wicks, C. McCallum, A.R. Kirmani, D.-H. Nam, C. Gabardo, A. Seifitokaldani, X. Wang, CO_2 electrolysis to multicarbon products at activities greater than 1 A cm^{-2}, Science 367 (2020) 661–666.

[3] A. Raya-Imbernon, A.A. Samu, S. Barwe, G. Cusati, T. Fodi, B.M. Hepp, C. Janaky, Renewable syngas generation via low-temperature electrolysis: opportunities and challenges, ACS Energy Lett. 9 (2024) 288–297.

[4] J. Pan, Y. Sun, P. Deng, F. Yang, S. Chen, Q. Zhou, H.S. Park, H. Liu, B. Yu Xia, Hierarchical and ultrathin copper nanosheets synthesized via galvanic replacement for selective electrocatalytic carbon dioxide conversion to carbon monoxide, Appl. Catal. B 255 (2019) 117736.

[5] L. Xue, C. Zhang, T. Shi, S. Liu, H. Zhang, M. Sun, F. Liu, Y. Liu, Y. Wang, X. Gu, S. Zeng, Unraveling the improved CO_2 adsorption and COOH* formation over Cu-decorated ZnO nanosheets for CO_2 reduction toward CO, Chem. Eng. J. 452 (2023) 139701.

[6] S.T. Guo, Y.W. Du, H. Luo, Z. Zhu, T. Ouyang, Z.Q. Liu, Stabilizing undercoordinated Zn active sites through confinement in CeO_2 nanotubes for efficient electrochemical CO_2 reduction, Angew. Chem. Int. Ed. Engl. 136 (2024) e202314099.

[7] K. Liu, J. Wang, M. Shi, J. Yan, Q. Jiang, Simultaneous achieving of high faradaic efficiency and CO partial current density for CO_2 reduction via robust, noble-metal-free Zn nanosheets with favorable adsorption energy, Adv. Energy Mater. 9 (2019) 1900276.

[8] W. Luo, Q. Zhang, J. Zhang, E. Moioli, K. Zhao, A. Züttel, Electrochemical reconstruction of ZnO for selective reduction of CO_2 to CO, Appl. Catal. B 273 (2020) 119060.

[9] H. Won da, H. Shin, J. Koh, J. Chung, H.S. Lee, H. Kim, S.I. Woo, Highly efficient, selective, and stable CO_2 electroreduction on a hexagonal Zn Catalyst, Angew. Chem. Int. Ed. Engl. 55 (2016) 9443–9446.

[10] A. Jo, S. Kim, H. Park, H.-Y. Park, J. Hyun Jang, H.S. Park, Enhanced electrochemical conversion of CO_2 to CO at bimetallic Ag-Zn catalysts formed on polypyrrole-coated electrode, J. Catal. 393 (2021) 92–99.

[11] F. Quan, D. Zhong, H. Song, F. Jia, L. Zhang, A highly efficient zinc catalyst for selective electroreduction of carbon dioxide in aqueous NaCl solution, J. Mater. Chem. A 3 (2015) 16409–16413.

[12] W. Luo, J. Zhang, M. Li, A. Züttel, Boosting CO production in electrocatalytic CO_2 reduction on highly porous Zn catalysts, ACS Catal. 9 (2019) 3783–3791.

[13] Z. Xing, L. Hu, D.S. Ripatti, X. Hu, X. Feng, Enhancing carbon dioxide gas-diffusion electrolysis by creating a hydrophobic catalyst microenvironment, Nat. Commun. 12 (2021) 136.

[14] H. Rabiee, M. Li, P. Yan, Y. Wu, X. Zhang, F. Dorosti, X. Zhang, B. Ma, S. Hu, H. Wang, Z. Zhu, L. Ge, Rational designing microenvironment of gas-diffusion electrodes via microgel-augmented CO_2 availability for high-rate and selective CO_2 electroreduction to ethylene, Adv. Sci. 11 (2024) 2402964.

[15] N.T. Nesbitt, T. Burdyny, H. Simonson, D. Salvatore, D. Bohra, R. Kas, W.A. Smith, Liquid–solid boundaries dominate activity of CO_2 reduction on gas-diffusion electrodes, ACS Catal. 10 (2020) 14093–14106.

[16] H. Rabiee, L. Ge, X. Zhang, S. Hu, M. Li, Z. Yuan, Gas diffusion electrodes (GDEs) for electrochemical reduction of carbon dioxide, carbon monoxide, and dinitrogen to value-added products: a review, Energy Environ. Sci. 14 (2021) 1959–2008.

[17] H. Rabiee, L. Ge, S. Hu, H. Wang, Z. Yuan, Microtubular electrodes: an emerging electrode configuration for electrocatalysis, bioelectrochemical and water treatment applications, Chem. Eng. J. 450 (2022) 138476.

[18] R. Kas, K.K. Hummadi, R. Kortlever, P. de Wit, A. Milbrat, M.W. Luiten-Olieman, N. E. Benes, M.T. Koper, G. Mul, Three-dimensional porous hollow fibre copper electrodes for efficient and high-rate electrochemical carbon dioxide reduction, Nat. Commun. 7 (2016) 10748.

[19] C. Zhu, Y. Song, X. Dong, G. Li, A. Chen, W. Chen, G. Wu, S. Li, W. Wei, Y. Sun, Ampere-level CO_2 reduction to multicarbon products over a copper gas penetration electrode, Energy Environ. Sci. 15 (2022) 5391–5404.

[20] H. Rabiee, L. Ge, J. Zhao, X. Zhang, M. Li, S. Hu, S. Smart, T.E. Rufford, Z. Zhu, H. Wang, Z. Yuan, Regulating the reaction zone of electrochemical CO_2 reduction on gas-diffusion electrodes by distinctive hydrophilic-hydrophobic catalyst layers, Appl. Catal. B 310 (2022) 121362.

[21] A. Chen, C. Zhu, J. Mao, S. Li, G. Wu, Y. Wei, X. Liu, X. Dong, Y. Song, G. Li, Y. Sun, W. Wei, W. Chen, Hollow penetration electrode of Bi with dislocated lattice enabling ampere-level reduction of CO_2 exclusively to formate, Appl. Catal. B 343 (2024) 123493.

[22] X. Dong, S. Li, C. Zhu, J. Mao, G. Wu, G. Li, G. Feng, A. Chen, Y. Wei, X. Liu, J. Wang, Y. Song, W. Chen, W. Wei, Highly efficient ampere-level CO_2 reduction to multicarbon products via stepwise hollow-fiber penetration electrodes, Appl. Catal. B 336 (2023) 122929.

[23] Y. Kuang, G. Chen, H. Rabiee, B. Ma, F. Dorosti, A.K. Nanjundan, Z. Zhu, H. Wang, L. Ge, Steering CO selectivity in CO_2 electroreduction over silver microtubular gas-diffusion electrodes via surface reconstruction, Energy Fuels 38 (2024) 10096–10105.

[24] G. Chen, L. Ge, Y. Kuang, H. Rabiee, B. Ma, F. Dorosti, A. Kumar Nanjundan, Z. Zhu, H. Wang, Hollow fiber gas-diffusion electrodes with tailored crystal facets for tuning syngas production in electrochemical CO_2 reduction, Chem. Eng. J. 490 (2024) 151651.

[25] G. Chen, L. Ge, Y. Kuang, H. Rabiee, B. Ma, F. Dorosti, A.K. Nanjundan, Z. Zhu, H. Wang, In situ growth of hierarchical silver sub-nanosheets on zinc nanosheets-based hollow fiber gas-diffusion electrodes for electrochemical CO_2 reduction to CO, Small Sci. 4 (2024) 2400184.

[26] H. Rabiee, L. Ge, X. Zhang, S. Hu, M. Li, S. Smart, Z. Zhu, Z. Yuan, Shape-tuned electrodeposition of bismuth-based nanosheets on flow-through hollow fiber gas diffusion electrode for high-efficiency CO_2 reduction to formate, Appl. Catal. B 286 (2021) 119945.

[27] H. Rabiee, X. Zhang, L. Ge, S. Hu, M. Li, S. Smart, Z. Zhu, Z. Yuan, Tuning the product selectivity of the Cu hollow fiber gas diffusion electrode for efficient CO_2 reduction to formate by controlled surface Sn electrodeposition, ACS Appl. Mater. Interfaces 12 (2020) 21670–21681.

[28] H. Rabiee, J.K. Heffernan, L. Ge, X. Zhang, P. Yan, E. Marcellin, S. Hu, Z. Zhu, H. Wang, Z. Yuan, Tuning flow-through cu-based hollow fiber gas-diffusion electrode for high-efficiency carbon monoxide (CO) electroreduction to C_{2+} products, Appl. Catal. B 330 (2023) 122589.

[29] J. Zhang, W. Luo, A. Züttel, Self-supported copper-based gas diffusion electrodes for CO_2 electrochemical reduction, J. Mater. Chem. A 7 (2019) 26285–26292.

[30] Z. Xing, X. Hu, X. Feng, Tuning the microenvironment in gas-diffusion electrodes enables high-rate CO_2 electrolysis to formate, ACS Energy Lett. 6 (2021) 1694–1702.

[31] J.A. Rabinowitz, D.S. Ripatti, R.G. Mariano, M.W. Kanan, Improving the energy efficiency of CO electrolysis by controlling Cu domain size in gas diffusion electrodes, ACS Energy Lett. 7 (2022) 4098–4105.

[32] Y. Wu, L. Charlesworth, I. Maglaya, M.N. Idros, M. Li, T. Burdyny, G. Wang, T. E. Rufford, Mitigating electrolyte flooding for electrochemical CO_2 reduction via infiltration of hydrophobic particles in a gas diffusion layer, ACS Energy Lett. 7 (2022) 2884–2892.

[33] W. Wang, K. Zhang, T. Xu, Y. Yao, Local environment-mediated efficient electrocatalysis of CO_2 to CO on Zn nanosheets, Dalton Trans. 51 (2022) 17081–17088.

[34] L.C. Weng, A.T. Bell, A.Z. Weber, Modeling gas-diffusion electrodes for CO_2 reduction, Phys. Chem. Chem. Phys. 20 (2018) 16973–16984.

[35] Q. Wan, B. Li, L. Li, Y. Liu, L. Yuan, E. Zhang, X. Zhuang, Y. Jiang, J. Zhang, C. Ke, Decoupling and quantifying the mass transfer resistance of the gas diffusion electrode for CO_2 electrochemical reduction reaction, Chem. Eng. J. 496 (2024) 154124.

[36] L. Xiong, X. Fu, Y. Zhou, P. Nian, Z. Wang, Q. Yue, Precise site-hydrophobicity modulation for boosting high-performance CO_2 electroreduction, ACS Catal. 13 (2023) 6652–6660.

[37] S. Li, X. Dong, J. Mao, W. Chen, A. Chen, G. Wu, C. Zhu, G. Li, Y. Wei, X. Liu, J. Wang, Y. Song, W. Wei, Highly efficient CO_2 reduction at steady 2 A cm^{-2} by surface reconstruction of silver penetration electrode, Small 19 (2023) 2301338.

[38] A. Chen, X. Dong, J. Mao, W. Chen, C. Zhu, S. Li, G. Wu, Y. Wei, X. Liu, G. Li, Y. Song, Z. Jiang, W. Wei, Y. Sun, Gas penetrating hollow fiber Bi with contractive bond enables industry-level CO_2 electroreduction, Appl. Catal. B 333 (2023) 122768.

[39] J. Xiao, M.R. Gao, S. Liu, J.L. Luo, Hexagonal Zn nanoplates enclosed by Zn(100) and Zn(002) facets for highly selective CO_2 electroreduction to CO, ACS Appl. Mater. Interfaces 12 (2020) 31431–31438.

[40] B. Qin, Y. Li, H. Fu, H. Wang, S. Chen, Z. Liu, F. Peng, Electrochemical reduction of CO_2 into tunable syngas production by regulating the crystal facets of Earth-abundant Zn catalyst, ACS Appl. Mater. Interfaces 10 (2018) 20530–20539.

[41] P. Yue, Q. Fu, J. Li, L. Zhang, L. Xing, Z. Kang, Q. Liao, X. Zhu, Triple-phase electrocatalysis for the enhanced CO_2 reduction to HCOOH on a hydrophobic surface, Chem. Eng. J. 405 (2021) 126975.

[42] K. Fan, Y. Jia, Y. Ji, P. Kuang, B. Zhu, X. Liu, J. Yu, Curved surface boosts electrochemical CO_2 reduction to formate via bismuth nanotubes in a wide potential window, ACS Catal. 10 (2020) 358–364.

[43] A. Salehi-Khojin, H.-R.M. Jhong, B.A. Rosen, W. Zhu, S. Ma, P.J. Kenis, R.I. Masel, Nanoparticle silver catalysts that show enhanced activity for carbon dioxide electrolysis, J. Phys. Chem. C 117 (2013) 1627–1632.

[44] Z. Geng, X. Kong, W. Chen, H. Su, Y. Liu, F. Cai, G. Wang, J. Zeng, Oxygen vacancies in ZnO nanosheets enhance CO_2 electrochemical reduction to CO, Angew. Chem. Int. Ed. Engl. 130 (2018) 6162–6167.

[45] K.P. Kuhl, T. Hatsukade, E.R. Cave, D.N. Abram, J. Kibsgaard, T.F. Jaramillo, Electrocatalytic conversion of carbon dioxide to methane and methanol on transition metal surfaces, J. Am. Chem. Soc. 136 (2014) 14107–14113.

[46] P. Moreno-García, N. Schlegel, A. Zanetti, A. Cedeño López, M.A.D.J.S. Gálvez-Vázquez, A. Dutta, M. Rahaman, P. Broekmann, Selective electrochemical reduction of CO2 to CO on Zn-based foams produced by Cu2+ and template-assisted electrodeposition, ACS Appl. Mater. Interfaces 10 (2018) 31355–31365.

[47] D.L.T. Nguyen, M.S. Jee, D.H. Won, H. Jung, H.-S. Oh, B.K. Min, Y.J. Hwang, Selective CO_2 reduction on zinc electrocatalyst: the effect of zinc oxidation state induced by pretreatment environment, ACS Sustain. Chem. Eng. 5 (2017) 11377–11386.

[48] J. Rosen, G.S. Hutchings, Q. Lu, R.V. Forest, A. Moore, F. Jiao, Electrodeposited Zn dendrites with enhanced CO selectivity for electrocatalytic CO_2 reduction, ACS Catal. 5 (2015) 4586–4591.
[49] T. Zhang, X. Li, Y. Qiu, P. Su, W. Xu, H. Zhong, H. Zhang, Multilayered Zn nanosheets as an electrocatalyst for efficient electrochemical reduction of CO_2, J. Catal. 357 (2018) 154–162.
[50] M.P.L. Kang, M.J. Kolb, F. Calle-Vallejo, B.S. Yeo, The role of undercoordinated sites on zinc electrodes for CO_2 reduction to CO, Adv. Funct. Mater. 32 (2022) 2111597.
[51] W. Lai, Y. Qiao, Y. Wang, H. Huang, Stability issues in electrochemical CO_2 reduction: recent advances in fundamental understanding and design strategies, Adv. Mater. 35 (2023) 2306288.
[52] J. Feng, J. Li, L. Qiao, D. Liu, P. Zhou, J. Ni, H. Pan, Reconstructed anti-poisoning surface for enhanced electrochemical CO_2 reduction on Cu-incorporated ZnO, Appl. Catal. B 330 (2023) 122665.